

# 1 Pulsed Laser Deposition for Complex Oxide Thin Film and Nanostructure

Chunrui Ma and Chonglin Chen

## 1.1

### Introduction

Complex oxide thin films and nanostructures are at the heart of new “oxide electronic” applications, such as ultraviolet light-emitting diodes [1–3], resistive switching memories [4, 5], chemical sensor [6, 7], and so on. They are often grown by pulsed laser deposition (PLD) because the technique is believed to be material agnostic. PLD is a thin film deposition technique – a type of physical vapor deposition. A high-power pulsed laser beam is focused on and strikes a target of the material that is to be deposited in a vacuum chamber. This material is vaporized from the target in a plasma plume and deposited as a thin film on a substrate. This process can occur in ultrahigh vacuum or in the presence of a background gas, such as oxygen, which is commonly used when depositing complex oxides.

The synthesis of novel thin films and structures is advancing on two fronts: one is the complexity of materials being deposited; and the other is the reduction in the typical dimensions of the features. As a rule of thumb, any structure that has one or more dimension smaller than about 100 nm is considered to be a nanostructured material. PLD is one of the most promising techniques for the formation of complex oxide heterostructures and nanostructures. The basic setup of PLD is simple relative to many other deposition techniques, and it can stoichiometrically transfer a material from a solid source to a substrate to form its thin film. The first use of PLD to deposit the films of semiconductors and dielectrics by ruby laser is reported in the literature as early as 1965 [8]. PLD for the film growth of  $\text{SrTiO}_3$  and  $\text{BaTiO}_3$  was achieved in 1969 [9]. Six years later, stoichiometric intermetallic materials ( $\text{Ni}_3\text{Mn}$  and  $\text{ReBe}_{22}$ ) were fabricated by using PLD [10]. In 1987, PLD had a real breakthrough in its successful application to the *in situ* growth of epitaxial high-temperature superconductor films at Bell Communications Research [11]. Since then, PLD has been used extensively in the growth of high-temperature cuprates and numerous other complex oxides, including materials that cannot be obtained by an equilibrium route [12–16].

This chapter details the PLD setup and focuses primarily on the operating principle, growth mechanism, and parameters of PLD for complex oxide thin film and nanostructure.

## 1.2

### Pulsed Laser Deposition System Setup

The technique of PLD is conceptually simple, as illustrated schematically in Figure 1.1. The system consists of a laser, a vacuum chamber equipped with pumps, a target holder and rotator, and a substrate heater and is typically equipped with various pressure gauges, controllers, and other instruments to control the deposition environment of the system [17]. Film growth can be carried out in reactive environments, such as that for oxides where a partial pressure of oxygen, ozone, or atomic oxygen is carefully controlled. The substrate heater controls the substrate temperature. PLD systems are also often equipped with a set of optics including apertures, attenuators, mirrors, and lenses to focus and direct the laser beam into the target with the right energy density. The bulk material target orients at an angle of  $45^\circ$  toward the incident laser beam. The laser beam is focused onto the target surface by a set of optical components. The target locally absorbs the laser pulse energy and ejects a small amount of target material in the form of a plume containing many energetic species including atoms, molecules, electrons, ions, clusters, particulates, and molten globules. The plasma is then deposited onto a substrate facing the target with a separation distance of 3–5 cm. The substrate temperature can be varied from room temperature to  $1000^\circ\text{C}$ , even higher than  $1000^\circ\text{C}$ , depending on the heater type. The film microstructure depends on various parameters such as substrate

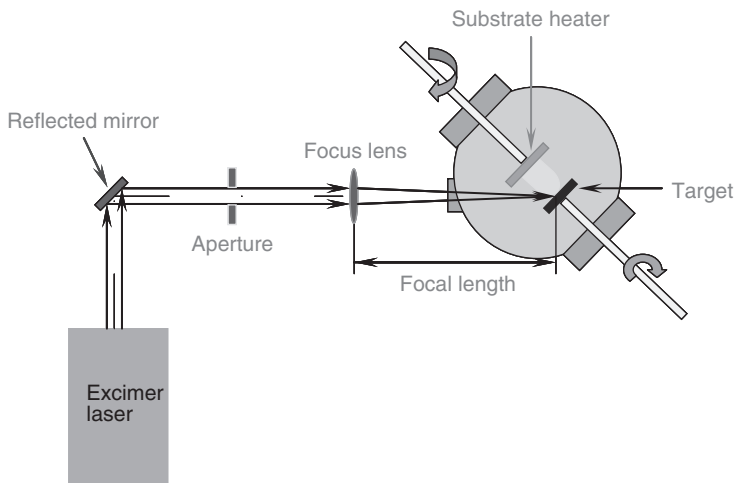


Figure 1.1 Schematic diagram of typical pulsed laser deposition.

temperature; laser energy density and pulse repetition rate; pressure and type of gas inside the chamber; and substrate-to-target distance.

### 1.3

#### **Advantages and Disadvantages of Pulsed Laser Deposition**

PLD exhibits many fascinating properties and practical advantages. Firstly, it has the ability to faithfully keep the stoichiometry of the target material, which is the first aspect that draws the attention of the thin film growth community [18]. Secondly, the energy source for material transport (i.e., the laser) is outside the chamber, minimizing any impurities caused by in-vacuum power components; it is very flexible, cost effective, and fast. Many different materials can be ablated by using the same apparatus, and the different laser wavelengths are available in principle. The isolated local heating by the laser spot means that several different materials can be sequentially ablated in a single vacuum chamber by using a carousel system or a segmented target rod to fabricate heterostructures with little of cross-contamination of the source target material. This avoids the interconnected vacuum transfer and is an important advantage in research environment: one laser can serve many vacuum systems in order to save the laser cost, and high-quality samples can be grown in 10 or 20 min. Finally, it is easy to control film thickness and multilayer film by controlling the pulse repetition rate, growth time, and the use of multiple target holders; it demands a much lower substrate temperature than other film deposition techniques because the high kinetic energy (10–100 eV) of species in the ablation plume promotes surface mobility during film growth.

In spite of the above-mentioned advantages of PLD, there are some drawbacks in using the PLD technique. One of the major problems is limited uniformity because the plasma plume ejected from the target can only provide a narrow forward angular distribution. Another problem is high defect or particulate concentration due to surface boiling. The size of particulates may be as large as a few micrometers, which will greatly affect the growth of the subsequent layers as well as the electrical properties of the films. Therefore, these features limit the large-scale film growth. New techniques, such as rotating both target and substrate and using a shadow mask to block the particulates in order to fabricate a large and uniform film, have been developed to improve the film quality.

### 1.4

#### **The Thermodynamics and Kinetics of Pulsed Laser Deposition**

PLD is a nonequilibrium growth technique owing to the high electronic excitation, degree of ionization, and kinetic energies of flux. There are many distinct stages to film growth: [19] the ablation process of the target material by the laser irradiation; the creation of a plasma plume with high energetic ions; and the crystalline

growth of the film itself on the heated substrate. In this section, we will thoroughly describe these processes.

#### 1.4.1

##### Laser–Material Interactions

After the laser pulse is extinguished, a very hot cloud of vaporized material, typically of  $10^4$  K or more, has been generated, which is commonly referred to as the *ablation plasma* or *plume*. This process is called *laser ablation*. The mechanisms depend on the laser characteristics as well as on the optical, topological, and thermodynamic properties of the target material. Absorption in a material is defined as

$$I = I_0 e^{-\alpha x}$$

where  $1/\alpha$  is the absorption length, which is approximately 100 nm for many oxide materials at laser wavelengths commonly used in PLD ( $<400$  nm). In this process, electrons in the target are excited and thermalized within several picoseconds or nanoseconds depending on the energy density, duration, wavelength, and shape of the laser pulse as well as on the material properties (reflectivity, absorption coefficient, heat capacity, thermal conductivity, density, etc.). The next step includes surface melting of the target and conduction of heat into the target. The thermal diffusion length is described as

$$\lambda_{\text{th}} = 2(\alpha_{\text{th}} \Delta t)^{1/2}$$

where  $\alpha_{\text{th}} = \frac{K}{\rho c}$  is the thermal diffusivity,  $K$  is the thermal conductivity,  $\rho$  is the mass density,  $c$  is the specific heat, and  $\Delta t$  is the pulse duration. During this process, the temperature rises in the surface of the target. The heating rates as high as  $10^{11}$  K/s and instantaneous gas pressures of 10–500 atm are observed at the target surface. Then, the target material will vaporize. During this step, there is multiphoton ionization of the gaseous phase creating the characteristic plasma and the temperature at the surface of the target will exceed the boiling point. The final step of the process is the plasma excitation during which further ionization occurs and free electrons are excited, resulting in Bremsstrahlung absorption in which the hot pulse, at nearly 2000 K, expands in a directed manner.

The ablation threshold of materials, or the minimum energy density required in a material to create a plume, will be discussed. In most oxides, the thermal diffusion length is much longer than the absorption length, especially for UV lasers, because of the fact that oxide materials are often opaque and good thermal conductors. An affected volume is related to the spot size times  $\lambda_{\text{th}}$ ; thus, a simple estimation of the minimum energy needed to raise this volume to the sublimation point is

$$Q_{\text{heat}} = C_S(T_{\text{melt}} - T) + \Delta H_m + C_m(T_{\text{vap}} - T_{\text{melt}}) + \Delta H_{\text{vap}}$$

where the total energy required (from left to right) is the sum of the energy needed to bring the target material to the melting temperature plus the heat of melting,

plus the energy needed to bring the melted material to the vaporization point, plus the heat of vaporization. Although this seems like a large amount of energy, a typical instantaneous power density for a single laser pulse with energy density of approximately  $2 \text{ J/cm}^2$  and 20 ns pulse duration is about  $10^8 \text{ W/cm}^2$ , which is more than enough to ablate nearly all materials.

#### 1.4.2

##### Dynamics of the Plasma

The material expands in a plasma form parallel to the normal vector of the target surface toward the substrate owing to Coulomb repulsion and recoil from the target surface. The plasma contains many energetic species such as atoms, molecules, electrons, ions, clusters, particulates, and molten globules with the typical plasma temperature around 10 000 K, above the boiling points of most materials. As the plasma expands, it adiabatically cools to 3000–5000 K. The spatial distribution of the plume is strongly dependent on the background pressure inside the PLD chamber. In vacuum, the plume is very narrow and forward directed; at intermediate pressure, it looks like a shock wave due to the splitting of high energetic ions from the less energetic ions; at high pressure, it undergoes a more diffusion-like expansion. The angular distribution of the plume has been fitted to a  $\cos^n(x)$  function, with the value of  $n$  ranging from 2 to more than 20. In general,  $n$  is lower when the plasma is at high pressure because multiple collisions broaden the angular distribution [20]. The propagation of the plasma in the background gas follows a distance–time relation described by a blast wave model:

$$R = \zeta_0 \left( \frac{E_0}{\rho_0} \right)^{1/5} t^{2/5}$$

where  $\zeta_0$  is a constant,  $\rho_0$  is the background gas density, and  $E_0$  is the kinetic energy. This model is valid when the mass of the ejected material is smaller than the mass of the background gas. Therefore, the background gas pressure in PLD must be kept at a very low level so that some of the ejected species can avoid being scattered by the background gas and reach the substrate successfully.

#### 1.4.3

##### Nucleation and Growth of the Film on the Substrate Surface

Nucleation and growth of the film are of importance to determine thin film quality, morphology, and stoichiometry [21]. Growth of thin films resulting from a supersaturated gas condensation is a nonequilibrium phenomenon governed by a competition between kinetics and thermodynamics. Nucleation only occurs when the nucleus size  $r$  is equal to or greater than the critical nucleus  $r^*$ , as shown in Figure 1.2. It is worth noting that  $\Delta G^*$  represents a critical energy barrier in the nucleation process. When an aggregate momentarily forms owing to thermodynamic fluctuation but the size of the cluster is smaller than  $r^*$ , it is unstable and will disappear by shrinking in size, lowering  $\Delta G$  in the process. Only clusters with

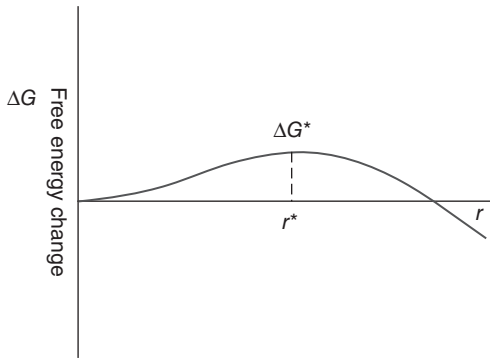


**Figure 1.2** Free energy as a function of cluster size  $r$ .  $r^*$  is the critical nucleus size and  $\Delta G^*$  is the critical free energy barrier for nucleation.

size larger than  $r^*$  can surmount the nucleation energy barrier, and they are stable and tend to grow larger in order to lower the energy of the system.

Kinetic processes in thin film nucleation on an ideal substrate surface [21, 22] are the impinging of the ablated high energetic species from the target onto the substrate surface and the sputtering off of some substrate atoms. These adatoms can subsequently diffuse over the substrate or along the island edge, encounter and bind with each other to form clusters, or attach to an existing island. On the other hand, they can also be re-evaporated from the substrate, from an island, or from a cluster. Meanwhile, it is possible that they are detached from the existing cluster edge but still remain on the substrate surface. In fact, the crystalline surface is not ideally flat but contains lots of defects and step terraces, so other kinetic processes such as interdiffusion and interfacial reactions become significant.

There are several factors that affect the film growth structure. First of all, the nucleation rate is an important parameter: high nucleation rates during deposition will encourage a fine-grained film or even amorphous structure. On the other hand, if nucleation is suppressed, single crystal growth is fostered. Substrate temperature is another factor to influence the film growth. Combining these two parameters, it is concluded that high substrate temperature and low deposition rates favor large crystallites or even monocrystal formation. Alternatively, low substrate temperatures and high deposition rates yield polycrystalline deposits. Basically, there are three thin film growth modes [22, 23]:

1. *Island or Volmer–Weber mode*: As shown in Figure 1.3a, island growth occurs when the smallest stable clusters nucleate on the substrate and grow in three dimensions to form islands. The growth of three-dimensional (3D) islands on the substrate is due to the fact that the bonds between the film atoms are stronger than the binding force of atoms to the substrate.
2. *Layer-by-layer or Frank–van der Merwe mode*: This kind of thin film growth mode (Figure 1.3b) occurs when the atoms are more strongly bound to the

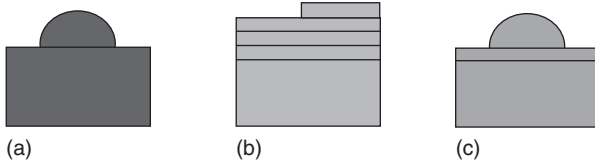


**Figure 1.3** Basic modes of thin film growth: (a) island or Volmer–Weber mode, (b) layer-by-layer or Frank–van der Merwe mode, and (c) layer plus island or Stranski–Krastanov mode.

substrate than to each other. Film atoms are completely coalescent to form a monolayer on the surface before they develop into significant clusters on the next layer owing to the no barrier nucleation on this 2D island formation [24, 25]. As long as the decrease in bonding energy is continuous toward the bulk crystal value, the layer growth mode is sustained.

3. *Layer plus island or Stranski–Krastanov mode* (Figure 1.3c): The layer plus island mode follows a two-step process: after forming one or more monolayers, namely, above a critical layer thickness, the layer-by-layer growth mode becomes 3D island forms. The transition mechanism from layer growth mode to island growth mode is unclear until now, but any factor that disturbs the monotonic decrease in binding energy may be the cause, such as the strain from the misfit between the thin film and the substrate, dislocation in the film, chemical potential of the deposited film, and so on.

It is known that the thin film growth mode also depends on the interfacial energies between the three phases present: the substrate, the condensing material, and the vapor [24].

$$\sigma_s < \sigma_{hkl} + \sigma_i - \frac{kT \ln s}{2k_{hkl} b^2} \quad (\text{island mode})$$

$$\sigma_s > \sigma_{hkl} + \sigma_i - \frac{kT \ln s}{2k_{hkl} b^2} \quad (\text{layer mode})$$

where  $\sigma_s$  and  $\sigma_i$  are the free energy of the substrate surface and interface, respectively,  $\sigma_{hkl}$  is the specific surface energy of the contact plane of the deposit, and  $b$  is the contact length.

In PLD systems, the nucleation process and growth kinetics of the thin film depend on several growth parameters: laser parameters (laser energy, pulse repetition rate), ionization degree of the ablated material, substrate temperature, substrate surface, and background pressure. Among them, the substrate temperature  $T$  and the supersaturation  $s$  are very important, defined by

$$s = \frac{R}{R_e}$$

where  $R$  is the actual deposition rate and  $R_e$  is the equilibrium deposition value at temperature  $T$ . A small supersaturation induces large nuclei, leading to island thin film growth mode. As the supersaturation increases, the critical nucleus keeps

shrinking to the atomic level, and then the impinging adatoms will be more likely to add directly to the edges of the existing clusters before they encounter other adatoms. Therefore, the high supersaturation value tends to promote the layer thin film mode [19, 26].

In addition to supersaturation, the substrate temperature also plays an important role in controlling the final microstructure and surface morphology of the as-grown film. At high temperatures, defects at the surface such as void, atomic step intersections, and dislocation intersections can be reduced and the crystallinity of the as-grown films can be improved. However, with the decrease in the substrate temperature, the surface diffusion coefficient decreases and the crystal structure formation slows down, resulting in disordered, or even amorphous, thin film structures.

## 1.5

### Monitoring of Growth Kinetics

#### 1.5.1

##### Introduction and RHEED Studies

In modern material science, the knowledge and control of the growth processes of oxide materials are important for the fabrication of high-quality epitaxial and heteroepitaxial thin film structures. The quality of a thin film is the key factor to determine its properties and application; thus, monitoring the film growth kinetics becomes the critical issue and has attracted much attention. In this section, we will briefly overview some methods to detect the film growth kinetics.

Reflection high-energy electron diffraction (RHEED) is a technique used to characterize the surface of crystalline materials. A RHEED system basically requires an electron source (gun), photoluminescent detector screen, and a sample with a clean surface. The electron gun generates a beam of electrons, which strikes the sample at a very small angle relative to the sample surface. Incident electrons are diffracted by atoms at the surface of the sample, and then a small fraction of the diffracted electrons interfere constructively at specific angles and form regular patterns on the detector. The diffraction pattern at the detector is a function of the sample surface because the electron interference is related to the position of atoms on the sample surface. A PLD system equipped with a RHEED system can monitor the growth of thin films. The intensities of individual spots on the RHEED pattern fluctuate in a periodic manner resulting from the relative surface coverage of the growing thin film. A simple model similar in shape to those used by film growth experts is shown in Figure 1.4. Each peak represents the formation of a new monolayer since the degree of order is at a maximum once a new monolayer has been formed. The overall intensity of the oscillations drops when more layers are grown because of the fact that the electron beam is focused on the original surface and gets out of focus as more layers are grown. Each full period corresponds to the formation of a single atomic

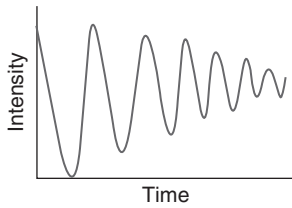


**Figure 1.4** The curve is a simple model of the fluctuation of the intensity of a single RHEED point during PLD.

layer thin film. The oscillation period is highly dependent on the material system, electron energy, and incident angle. Thus, RHEED has been widely applied to monitor the growth of complex oxide thin films, especially superlattices such as SrTiO<sub>3</sub> [27], YBa<sub>2</sub>Cu<sub>3</sub>O<sub>7-x</sub> [28], and superlattice LaAlO<sub>3</sub>/SrTiO<sub>3</sub> [29].

### 1.5.2

#### Growth Kinetics Studies by Surface X-ray Diffraction

Although RHEED is a tool for growth kinetics studies, the strong interaction of the electrons with the surface causes multiple scattering and requires a dynamic theory for rigorous interpretation of the intensities. As an alternative technique, surface X-ray diffraction (SXR) has the unique advantage that kinematic scattering is applicable and the intensity can be interpreted directly by surface coverage [30, 31]. Time-resolved SXR at crystal truncation rod (CTR) positions allows real-time measurements of interface layer formation; thus the combination of SXR and PLD is a powerful technique for gathering unique information on interface formation and growth kinetics. In addition, X-rays can avoid surface charging, making it the most suitable technique for studying oxide surfaces and interfaces. Unlike electrons, X-rays are not scattered by the high-pressure background, which is necessary in oxide growth, and do not interact with the surface or alter the growing film. Taking SrTiO<sub>3</sub> thin film as an example, the scattered intensity is measured simultaneously at the specular ( $00\frac{1}{2}$ ) and off-specular ( $01\frac{1}{2}$ ) CTRs before, during, and after PLD growth of SrTiO<sub>3</sub>. Measuring both rods is significant and can get the information about deposition, such as the height distribution of material, since the specular rod has momentum transfer along the surface normal. The lateral ordering on the surface and in-plane registry with the lattice that is synonymous with crystal growth are confirmed by measuring an off-specular rod ( $h, k \neq (0,0)$ ), which has an in-plane momentum transfer component. Well-developed and persistent RHEED-like SXR growth oscillations are observed simultaneously at both specular and off-specular CTR positions during homoepitaxial growth of SrTiO<sub>3</sub> at temperatures from 310 to 780 °C. The time resolution of 10 μs in SXR has the ability to measure the crystalline layer formation on the same timescale as the plume arrival time and reveals new details, which advance our understanding and change the transitional view of how PLD works.

## 1.6

### Fundamental Parameters in Thin Film Growth

It is well known that many parameters, such as substrate temperature, background gas, pre- and post-treatment, as well as the lattice misfit between the film and the substrate, can significantly influence the microstructure, defect density, epitaxial quality, and interface/surface morphology of the as-grown films. However, the optimum deposition conditions for excellent highly epitaxial thin films and the desired physical properties are still semi-empirical and require intense investigations. Therefore, in this section, we will mainly discuss the influence of substrate temperature, background gas, laser energy, target–substrate distance, post-annealing, and lattice misfit on thin-film quality.

#### 1.6.1

##### Substrate Temperature

Substrate temperature greatly determines the crystal structure, orientation, stoichiometric composition, and morphology of the as-grown film [32]. For a highly epitaxial single-crystalline phase, the deposition temperature should be in epitaxial temperature zone III, which is usually when the ratio of the deposition temperature to the melting point of the deposited material is above 0.5. High deposition temperatures can increase the surface mobility of the absorbed atoms and the crystallization rate, thus benefiting the epitaxial film growth. However, if substrate temperature is too high, the interdiffusion reaction between film and substrate and the substrate reconstruction may induce more distortion, thus reducing single crystallinity of the film. Sometimes, even within the optimal growth temperature range, different substrate temperatures can result in different crystal structures and film orientations. Therefore, suitable substrate temperature is an extremely important factor to determine the quality of the film. In addition, Sambri *et al.* reported that substrate temperature can significantly influence the plume dynamics of  $\text{La}_{0.7}\text{Sr}_{0.3}\text{MnO}_3$  and  $\text{SrTiO}_3$  and observed that a considerable reduction of the background gas resistance to plume propagation as the substrate temperature was increased, leading to a remarkable change in the velocity of species impacting the substrate during film growth and in their stopping distance. At the same time, they argued that the effect can be safely expected to be universal [33].

#### 1.6.2

##### Background Gas Pressure

Energetic species can be deactivated or quenched by collisional processes with a background gas [34]. The ideal range of energies of depositing species for promoting surface diffusion on the growing film is between about 10 and 40 eV. Although PLD produce a deposition flux just in this energy region, it tends to have high-energy tails that can result in implantation and produce significant disruption of film crystallinity. Therefore, introducing a background gas (especially oxygen gas

for oxide thin film) in PLD makes the entire kinetic energy distribution shift to lower values, which is a critical factor in controlling the stoichiometry and stabilizing the desired crystal phase in thin film growth [34]. Firstly, the background gas affects all the plume species and reduces their effectiveness in promoting surface diffusion. Secondly, the background gas pressure increases the deposition rate, especially for species such as Ba, Sr, Pb, and Ag, which show large re-sputtering yields, but decreases other species' deposition rate because the plume is strongly scattered by the gas and becomes less directed [35, 36]. Thirdly, too low oxygen pressures can lead to stress, usually compressive, in the film [37], caused by the bombardment of the film during the deposition by highly energetic species originating from the plume. High oxygen pressures, however, need higher deposition temperatures and, therefore, improved crystallinity is expected. Finally, an oxygen background is needed to ensure stoichiometric transfer from the target to the film. If the partial pressure of oxygen is too low, the film will grow off stoichiometry, which will affect the nucleation density and film quality. On the other hand, if the applied oxygen pressure is too high, the velocities of various species in the plume will be slowed down due to collisions with the oxygen molecules. Therefore, optimal oxygen pressure is necessary for getting a uniform and stoichiometric thin film.

### 1.6.3

#### Laser Fluence and Ablation Area

Laser fluence and ablation area are critical factors to control the stoichiometry. Inadequacy of either the laser fluence or the ablation area (the beam spot area) results in nonstoichiometric transfer of material from the ablation target [38]. Therefore, proper simultaneous choice of ablation laser fluence and ablation area is essential and often more important than the growth temperature and oxygen pressure for obtaining bulk-like properties in oxide heterostructures [39]. Ngom *et al.* reported the photographic imaging of plasma generated by KrF excimer laser ablation of  $\text{Sm}_{0.55}\text{Nd}_{0.45}\text{NiO}_3$  and investigated the effect of plasma dynamics on the growth of  $\text{Sm}_{0.55}\text{Nd}_{0.45}\text{NiO}_3$  solid solution during PLD [40]. The increase in the laser fluence can enhance the total optical emission of ZnO thin film [41]. Also, the ablation laser fluence has a very strong effect on the lattice constant and defect structure of the films, and  $0.3 \text{ J/cm}^2$  is the critical laser fluence, not threshold value, for stoichiometric  $\text{SrTiO}_3$  film growth [38].

### 1.6.4

#### Target–Substrate Distance

For most materials, the most important deposition parameters are the ambient  $\text{O}_2$  pressure ( $P$ ) and the substrate temperature ( $T_s$ ). It has been shown that the equilibrium  $P$ – $T_s$  phase diagram is a good guide for fabricating the *in situ* structural phase of the deposited oxides [42]. One of the major problems in PLD technology is spatial uniformity of the deposited films, which is related

to a peaked angular distribution of plasma arriving on the substrate. At a characteristic target–substrate distance ( $D$ ), the plasma loses its unidirectional velocity, scatters, and thermalizes, and this distance provides the optimum conditions for film growth. Several works have investigated experimentally and theoretically the relationship between  $P$  and  $D$  [43], which show that the  $P$ – $D$  correlation is more stringent than the  $P$ – $T_s$  requirement, since a slight deviation can cause a significant change in the film quality. A scaling law  $PD^3 = \text{constant}$  from thermodynamic data and the experimental volumetric erosion rate of the metallic elements ejected from the target was proposed in 2005 and successfully applied to the growth of  $\text{CdTeO}_3$ ,  $\text{AlVO}_4$ , and  $\text{PbFe}_{12}\text{O}_{19}$  [44].

### 1.6.5

#### Post-Annealing

Post-annealing has a great effect on the microstructure and local structure of films and is critical in order to obtain high-quality films [45]. ZnO thin films were post-growth annealed in air at various annealing temperatures for 30 min. Increasing the annealing temperatures favors the diffusion of atoms absorbed on the substrate and accelerates the migration of atoms to an energy-favorable position, resulting in enhancement of the crystallinity and  $c$ -axis orientation of ZnO films [46].

It is commonly observed that annealing in vacuum or a reducing atmosphere results in oxygen vacancies in complex oxide thin films and enlarges the lattice constant [47]. On the other hand, annealing in oxygen atmosphere will insert the oxygen into the film and reduce the lattice constant [48]. Hundley *et al.* reported that after the  $\text{La}_{0.7}\text{Ca}_{0.3}\text{MnO}_3$  thin film was fabricated, it was annealed in flowing oxygen at 950 °C for 10 h, which raised the Curie temperature, dropped resistivity by two or three orders of magnitude, and sharpened the magnetic signature of the ferromagnetic transition [49]. However, transition metal-doped ZnO thin film annealed in vacuum or a reducing atmosphere results in enhanced ferromagnetism of the sample due to the introduction of oxygen vacancies, with interstitial Zn critical for room temperature ferromagnetism in transition metal-doped ZnO [45].

### 1.6.6

#### Lattice Misfit

When thin films are grown on a single crystal substrate, two types of epitaxy can be distinguished and each has important scientific and technological implications [32]. Homoepitaxy refers to the case where the film and substrate are of the same material, such as epitaxial Si deposited on Si wafers. Heteroepitaxy is the second type and refers to the case where films and substrates are of different materials, which have a different crystal structure and lattice constant. An important quantity to characterize heteroepitaxy is the lattice misfit  $f$  defined as

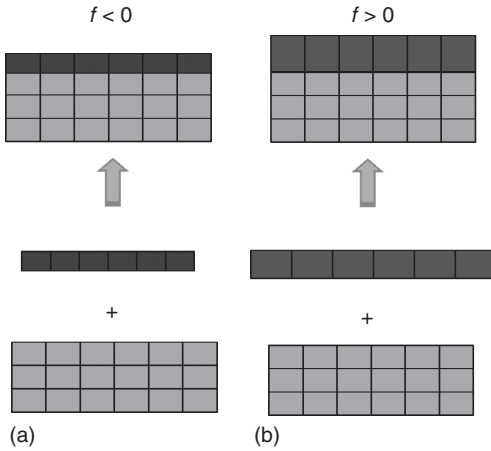


**Figure 1.5** Schematic representation: (a) the mismatch between the film and the substrate is negative; (b) the mismatch is positive.

$$f = \frac{a_f - a_s}{a_s}$$

$a_f$  and  $a_s$  are the unstrained lattice constants of the film and the substrate, respectively. A negative  $f$  (lattice constant of the film smaller than that of the substrate) implies that the initial layers of the epitaxial film will be stretched in tension (Figure 1.5a), and a positive  $f$  (lattice constant of the film larger than that of the substrate) means the film is under compression (Figure 1.5b).

Differences in lattice constant and thermal expansion behavior between the film and the underlying substrate will be imparted into strain in thin films [50], which will influence the physical properties and quality of thin films. A good lattice match between the substrate and the film can minimize the interface energy, especially the electrostatic repulsion potential, thus making epitaxial film growth occur easily. Usually, a small lattice mismatch value of less than 5% is required for epitaxial film growth. The small lattice mismatch correspondingly ensures small strain energy at the interface and leaves the film homogeneously strained and commensurate with the substrate.

## 1.7

### Pulsed Laser Deposition for Complex Oxide Thin Film Growth

PLD has been widely used to fabricate complex oxide thin films because of the above-mentioned advantages. In this section, we will focus on the PLD for complex oxide thin film growth, such as ferroelectric, ferromagnetic, and other functional oxide thin films. Also, we will discuss the film thickness, lattice mismatch, and post-annealing effect on the properties of complex oxide thin films.

## 1.7.1

**Pulsed Laser Deposition for Superconductor Thin Film**

Since 1987, PLD has been extensively applied to the *in situ* growth of epitaxial high-temperature superconductor films [11, 51–54]. In 1996, Norton *et al.* reported that *c*-axis-oriented  $\text{YBa}_2\text{Cu}_3\text{O}_7$  films with superconducting critical current density as high as  $700\,000\text{ A/cm}^2$  at 77 K were fabricated on thermomechanically rolled textured nickel (001) tapes by PLD, which is comparable to those grown on single crystal oxide substrates. This result represents a viable approach for the production of long superconducting tapes for high-current, high-field application at 77 K by PLD [55]. Later on, PLD is widely used to fabricate various superconductor thin films and improve the superconductor properties by interface strain, such as copper oxides,  $\text{La}_{2-x}\text{Sr}_x\text{CuO}_4$  [56],  $\text{SmBa}_2\text{Cu}_3\text{O}_y$  [57], and so on.

## 1.7.2

**Pulsed Laser Deposition for Ferroelectric Thin Films**

Ferroelectric oxide thin films, especially those grown by PLD, have fascinated scientists and engineers because of their interesting physical properties and important application in various areas, such as ferroelectric memories, ferroelectric field effect transistors, optical, microwave devices, and so on [58–60]. Lead zirconate titanate (PZT) has long been the leading material considered for ferroelectric memories, though strontium bismuth tantalite (SBT) is also a popular choice because of its superior fatigue resistance and the fact that it is lead free [61].

Ferroelectric thin film as the gate of ferroelectric field effect transistors has been widely investigated and reviewed [58, 62, 63]. A ferroelectric transparent thin film transistor was fabricated by PLD, consisting of a high-mobility, Sb-doped, n-type  $\text{SnO}_2$  semiconductor layer:  $\text{PbZr}_{0.2}\text{Ti}_{0.8}\text{O}_3$  as a ferroelectric insulator and  $\text{SrRuO}_3$  as a gate electrode [62]. It is found that a pulse of small voltage (3 V) can induce a change in the remnant conductance by a factor of 2. Also, epitaxial cuprate superconductor ferroelectric heterostructures were investigated by PLD [64].

In the past two decades, ferroelectric barium strontium titanate ( $\text{Ba}_x\text{Sr}_{1-x}\text{TiO}_3$ ) thin films have been considered to be one of the most important candidates for microwave elements because the dielectric constant can be tuned by an external field and the Curie temperature can be adjusted by varying the solution concentration between barium titanate and strontium titanate. Chen *et al.* recently systematically investigated the microwave properties of epitaxial BST or doped BST by fabricating single-layered or multilayered ferroelectric thin films. The tenability can reach 62% at 2G frequency by interface strain from the substrate, which is the maximum value reported in the literature [65–70].

It is known that the interface strain can significantly influence the properties of thin films, especially the perovskite structure's ferroelectric thin film. Predictions

and measurements of the effect of biaxial strain on the properties of epitaxial ferroelectric thin films and superlattices were reviewed in 2007 [71].

### 1.7.3

#### Pulsed Laser Deposition for Ferromagnetic Thin Film

Ferromagnetic oxide thin films fabricated by PLD, such as perovskite manganites, cobaltates, and ion oxides, have been intensively investigated worldwide over the past several decades because they span a wide range of crystal structure and exhibit an incredible variety of physical phenomena and spectacular functionality, for example, magnetic storage, sensors and activators, spintronic and colossal magnetoresistance (CMR), and so on [72, 73].

Perovskite cobaltates with a chemical formula  $(Ln, A)CoO_{3-\delta}$  ( $Ln$  = lanthanide,  $A$  = alkaline earth metal: Ca, Sr, or Ba) have recently attracted significant interest owing to important magnetic and electronic transport properties such as CMR, magnetic ordering, electronic phase separation, insulator–metal transition, and large thermoelectric power at low temperatures. These properties offer various application prospects, that is, magnetic data storage, oxidation catalyst, fuel cell cathode, gas sensor, and so on [74–76]. Chen *et al.* recently systemically investigated an epitaxial  $LaBaCo_2O_{5+\delta}$  (LBCO) thin film, fabricated by PLD, from high-temperature fuel cell properties to low-temperature magnetic properties by interface strain; it is found that the magnetoresistance of epitaxial LBCO thin film is almost three times that of the bulk materials and increases the application temperature from 10 to 40 K [77–79]. Also, a series of transparent ferromagnet thin films, that is,  $Sn_{0.95}Fe_{0.05}O_2$ , were fabricated by PLD [80].

### 1.7.4

#### Pulsed Laser Deposition for Multiferroics Thin Film

Multiferroics is magnetism and ferroelectricity coexisting in materials and the quest for multiferroic materials is of great technological and fundamental importance since magnetism and ferroelectricity are essential to many forms of current technology [81, 82]. PLD system has been widely applied to fabricate not only the single-phase multiferroic thin film but also the horizontal and vertical heterostructures. To our knowledge, only two classes of single-phase multiferroic hexagonal manganites and the Bi-based perovskites have been prepared as single-phase films. The first multiferroic to be investigated in thin film form was the hexagonal manganite  $YMnO_3$  [83, 84]. Currently, perovskite structure bismuth ferrite is the most studied single-component multiferroic because of its high Curie temperature (820 °C) and large polarization, making it appealing for application in ferroelectric nonvolatile memories and high-temperature electronics [85, 86].

Horizontal heterostructures consisting of alternating layers of conventional ferromagnets and ferroelectrics [87], such as  $Pr_{0.85}Ca_{0.15}MnO_3$  and  $Ba_{0.6}Sr_{0.4}TiO_3$  superlattice, have been reviewed elsewhere [88]. Vertical heterostructures such

as the nanopillar geometry, recently, have attracted much attention owing to the reduced substrate-imposed mechanical clamping and larger interfacial surface area in three dimensions, which allows for stronger coupling between ferroelectric and magnetic components [89]. Although many different combinations of perovskite ( $\text{BaTiO}_3$ ,  $\text{BiFeO}_3$ ,  $\text{PbTiO}_3$ ) and spinels ( $\text{CoFe}_2\text{O}_4$ ,  $\text{NiFe}_2\text{O}_4$ , and  $\text{Fe}_3\text{O}_4$ ) have been grown, the design and control of such heterostructures remain a challenge.

### 1.7.5

#### Interface Strain Engineering the Complex Oxide Thin Film

It is well known that strain engineering in the complex oxide thin film has received considerable interest owing to its significant impact on the microstructure and physical properties of epitaxial thin film for several decades [90–96]. Interesting and anomalous new electrical and magnetic properties can be achieved by strain modification, such as with superconducting thin films grown on different substrates. The influence of lattice distortions on the magnetic properties of perovskite-related manganite films has been established both theoretically and experimentally [91, 97, 98].

##### 1.7.5.1 Thickness Effect

The thickness of a thin film is among the first quoted attributes of its nature because physical properties and behaviors of the thin film, as well as crystal structures, are strongly dependent on its thickness. In general, for very thin films, the material will adapt itself to the structure imposed by the substrate. At the same time, the thin film stores the biaxial strain energy below a critical thickness because of the lattice mismatch between the film and the substrate. With thin film growth, the strain energy will be rapidly accumulated and stored in the film. When the thickness of the thin film is above the critical thickness, edge dislocations are usually formed to fully or partially release the strain, so the influence of the substrate diminishes and the material adopts the structure of the bulk, with the lattice constant of the thin film being equal or close to its bulk lattice constant under similar growth conditions. It is evident that a thin film with thickness less than the critical thickness will have obviously different physical properties from those with a larger thickness. Highly epitaxial LBCO thin films on (001) MgO are systematically investigated as a function of the thin film thickness and a 7-nm strained layer is observed, which is marked in Figure 1.6(e) below the black line [77].

As shown in Figure 1.7a, the resistivity of the films and the metal–insulation transition temperature increase rapidly with decreased thickness because of the interface strain from the lattice misfit. In Figure 1.7b, the variable range hopping model fits better than the other two models in the  $40\text{ K} \leq T \leq 146\text{ K}$  range, suggesting that the LBCO is dominantly a disordered system in which the charge carriers move by hopping between various localized electronic states [99].

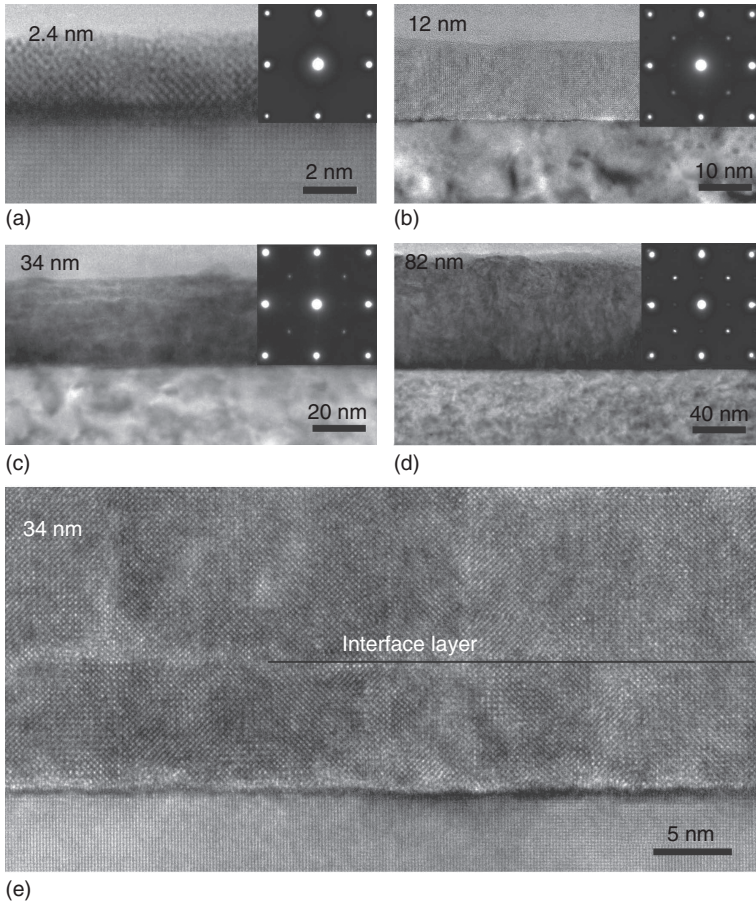


**Figure 1.6** (a–d) Transmission electron microscopic images for four different thicknesses of LBCO thin films on the MgO substrate and (e) cross-sectional

high-resolution transmission electron microscopy for 34-nm thin film. (Ma *et al.* [77]. Reproduced with permission of American Institute of Physics.)

### 1.7.5.2 Substrate Effect

Substrate is another very important factor engineering thin film structure and physical properties such as the Curie temperature shift, interface dislocation, and formation of nanocolumns. Selecting different substrates will produce either tensile strain or compressive strain in the thin film, which will influence the physical properties performance of a material. Consider a highly epitaxial LBCO thin film on four different substrates, (001)  $\text{LaAlO}_3$  (LAO), (001)  $\text{SrTiO}_3$  (STO), (110)  $\text{NdGaO}_3$  (NGO), and (001)  $\text{MgO}$ , as example; the LBCO film is under tensile strain on  $\text{MgO}$  and  $\text{STO}$  substrates while LAO and NGO impose compressive strain on it [79]. As shown in Figure 1.8, the film/substrate lattice mismatch can significantly affect the electrical conductivity and magnetoresistance of the

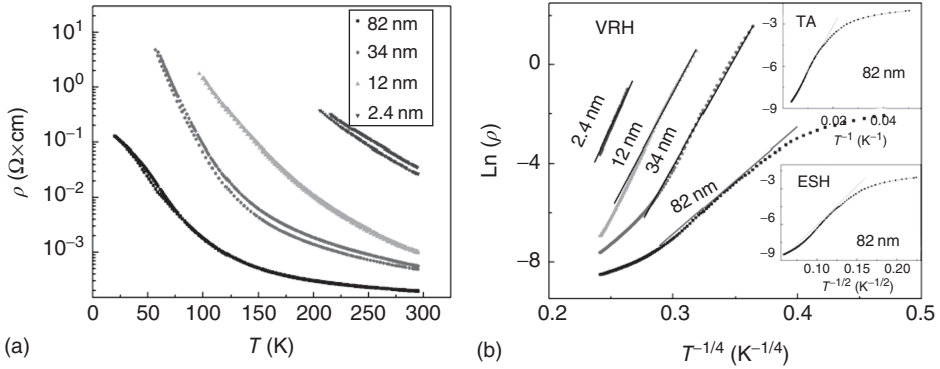


**Figure 1.7** (a) Temperature dependence of resistivity with different thickness and (b) logarithm of resistivity versus  $T^{-1/4}$  plot. Insets in (b): logarithm of the resistivity versus  $T^{-1/n}$  plots (where  $n = 1, 2$ ) for 82-nm LBCO thin film on MgO substrate. (Ma *et al.* [77]. Reproduced with permission of American Institute of Physics.)

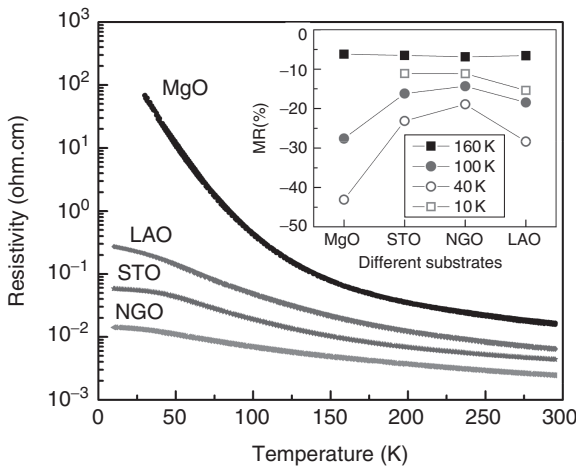


**Figure 1.8** Temperature dependence of the resistivity for LBCO thin films on various substrates. (Ma *et al.* [78]. Reproduced with permission of American Chemical Society.)

LBCO films. The resistivity for the LBCO thin film system is found to have the highest resistivity value on the MgO substrate, followed by the LAO, STO, and NGO in accordance with the sequence of the interface strain values. The large interface strain also induces the maximum magnetoresistance value of 43% for the LBCO films on the MgO substrates, which is almost three times that of the bulk materials, and increases the application temperature from 10 to 40 K.

In addition to the strain generated from the lattice mismatch between the substrate and the LBCO film, substrate surface structures such as surface step, terrace, and kink sites as well as other defect distribution are also important factors that

affect the microstructures and physical properties of the films. Only by carefully choosing the substrate's miscut angle (vicinality) can the step-flow growth be promoted, resulting in atomically smooth film surfaces. Chen *et al.* have systematically reported the magnetic and electrical transport properties of highly epitaxial LBCO thin films on vicinal (001) SrTiO<sub>3</sub> substrates with different miscut angles (0.5°, 3.0°, and 5.0°) and observed various interesting electronic transport properties and anomalous magnetic phenomena [78].

As shown in Figure 1.9, the electrical resistance of the LBCO films and the metal–insulation transition temperature decrease rapidly with increase in the miscut angles of vicinal (001) SrTiO<sub>3</sub> substrates. Magnetoresistance measurements were performed for the as-grown LBCO films as a function of the magnetic field ranging from 0 to 7 T using isothermal MR measurements. The MR is defined as  $MR(\%) = (\rho(H) - \rho(0)) / \rho(0) \times 100\%$ , where  $\rho(H)$  and  $\rho(0)$  are the resistivities with applied magnetic field and zero magnetic field, respectively. Obviously, the MR value of the LBCO on 0.5° miscut (001) SrTiO<sub>3</sub> is much larger than those on the other two vicinal substrates from the inset of Figure 1.9. The maximum MR value of approximately 34% is achieved at 60 K, which is much larger than the maximum value of 15% from its bulk material at 10 K [100], or the maximum value of 24% for the films grown on the regular (001) SrTiO<sub>3</sub> [101], which is represented as 0° in Figure 1.9.

They proposed a model to explain these phenomena as shown in Figure 1.10. When a number of film unit cells fill up along the terrace, a mismatch gap can be generated at the end of the step terrace (i.e., the “residual mismatching gap”), as seen in Figure 1.10a. Practically, this residual mismatch gap will not exist at

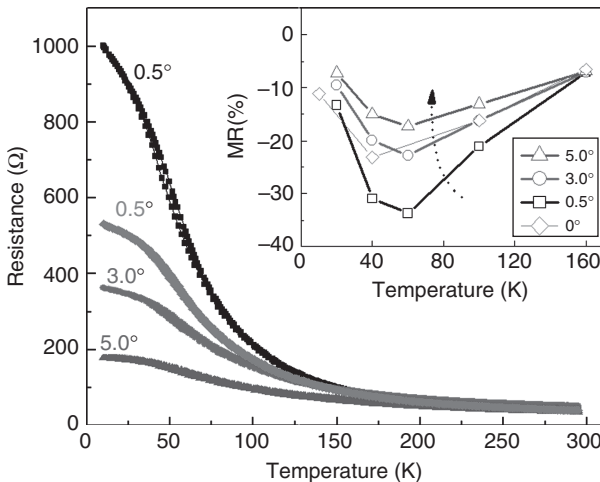


**Figure 1.9** Temperature dependence of resistance from 300 to 20 K for the as-grown LBCO thin films on different miscut angle (001) SrTiO<sub>3</sub> substrates. The inset is the MR

value of as-grown LBCO at different temperatures under 7 T magnetic field. (Ma *et al.* [78]. Reproduced with permission of American Chemical Society.)

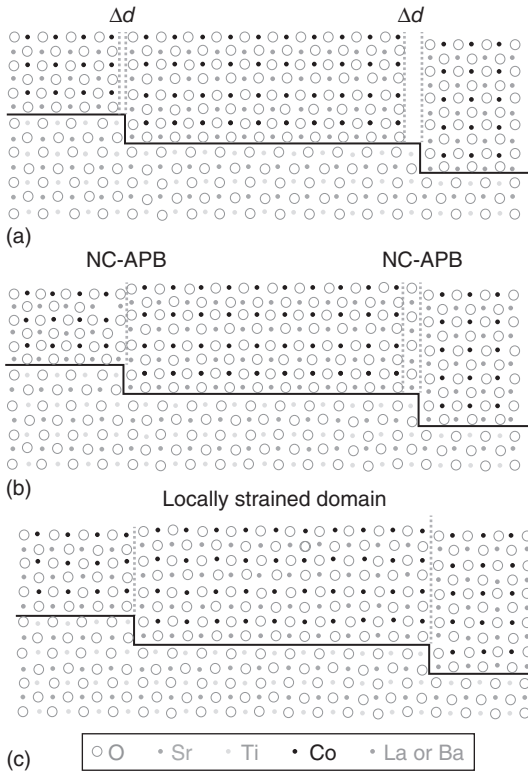


**Figure 1.10** The thin film/substrate mismatch in the epitaxial LBCO film grown on the vicinal (001)  $\text{SrTiO}_3$  substrates with low miscut angle: (a) the generation of the “residual mismatching gap” at the end of the step terrace; (b) the formation of nonconservative antiphase domain boundary; and (c) the formation of locally strained domains induced by the “residual mismatching gap.”

the end of the step terrace in an epitaxial film. The last atomic plane of the film will always occupy the atomic position of the terrace end by rearranging the local atomic structure. Two possible atomic rearrangements for the highly epitaxial oxide thin films can be considered: the formation of nonconservative antiphase domain boundary [102] and that of the locally strained domain induced from the “residual mismatching gap,” as seen in Figure 1.10b,c. For the half unit cell residual mismatching gap, it is highly improbable to form a nonconservative antiphase domain boundary at the end of the substrate terrace since a huge amount of interface strain energy will be generated because of the same charge repulsion at the domain boundary and interface. Therefore, the residual matching gap will be released via the formation of a locally strained domain, resulting in tensile strain over the interface and compressive strain along the out-of-plane direction. The local strain can significantly alter the epitaxial quality and the resulting physical properties [103].

As seen in Figure 1.9, the resistance behavior for the film on the  $0.5^\circ$  miscut surface is more like semiconductors rather than the semimetallic behavior found for the films on the  $3.0^\circ$  and  $5.0^\circ$  vicinal surfaces, resulting from the larger tensile strain in  $0.5^\circ$  miscut surface, which induces distortion of the  $\text{CoO}_6$  octahedral structure and change of the Co–O bond length and Co–O–Co bond angles, reducing the hopping of the charge carriers hopping.

### 1.7.5.3 Post-Annealing

Complex oxide thin films are very sensitive to oxygen stoichiometry, since different oxygen content will induce various crystal structures and directly influence the properties of complex oxide thin films [46, 48]. Similar to cobalt oxides, cobalt has three valencies ( $\text{Co}^{2+}/\text{Co}^{3+}/\text{Co}^{4+}$ ) and various spin states, which are related to the content of oxygen inside. Oxygen stoichiometry, thus, is an important factor in determining Co ion coordination (octahedral or pyramidal), the Co spin state, the metal–insulator transition, as well as magnetic and electronic transport properties of the perovskite-based cobalt oxides. For higher cobalt valency, the material easily exhibits metallic ferromagnetic behavior and a metal–metal transition, whereas for lower cobalt valency one obtains weakly ferromagnetic semiconductors [104].

Highly epitaxial LBCO thin films were annealed at  $465^\circ\text{C}$  in a tube furnace under pure oxygen (1 atm) for 5 h to examine the post-annealing effect, especially oxygen effect. From Figure 1.11, both the as-grown and oxygen-annealed thin films show excellent single crystal quality. The only difference is that the peak positions are shifted slightly to a higher angle by annealing the thin film in oxygen flow (see the inset (a) of Figure 1.11 for the (200) diffraction peak), suggesting that

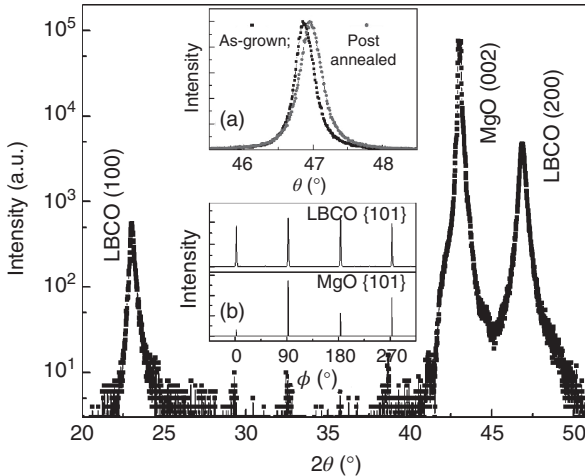


**Figure 1.11** A typical XRD pattern of the as-grown LBCO thin films on (001) MgO substrates. The inset (a) shows the (200) diffraction peaks of the as-grown and the

oxygen-annealed thin films. The inset (b) shows the  $\phi$  scans taken around the (101) diffraction of the LBCO thin films and MgO substrates.

the lattice parameter along the  $a$ -axis becomes smaller in the oxygen-annealed thin films because of the increase in the oxygen content, the decrease in the oxygen vacancies, and the increase in the attractive force between the anion and the cation.

Figure 1.12a shows that both oxygen-annealed and as-grown LBCO thin films exhibit spontaneous magnetizations  $M$  below approximately 170 K, but the magnetic moment of the oxygen-annealed sample is much higher than that of the as-grown sample, resulting from the increase in  $\text{Co}^{4+}$ , followed by the increase in double exchange of  $\text{Co}^{4+}\text{-O-Co}^{3+}$ . The resistivities of the as-grown and

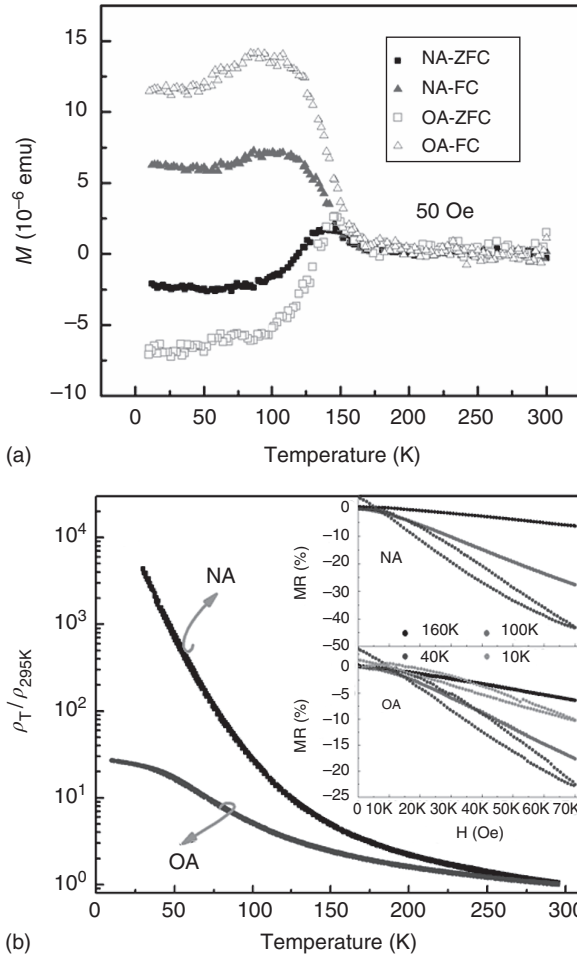


**Figure 1.12** (a) ZFC and FC magnetization of no annealing and oxygen annealing of LBCO thin film on (001) MgO substrate. (b) Resistivity change for the two samples

with temperature. Inset is the applied magnetic field dependence of the MR effects at isothermal magnetoresistance measurements.

oxygen-annealed samples increase exponentially with decreasing temperature, indicating both of them to be semiconductors. However, the resistivity for the oxygen-annealed thin film exhibits a semimetallic behavior below 50 K (Figure 1.12b). These phenomena indicate that post-annealing is a critical factor to influence the crystalline structure and physical properties of complex oxide thin films.

## 1.8

### Pulsed Laser Deposition for Nanostructure Growth

Miniaturization of electronic devices, such as the nanoscale design of memories, sensors, and actuators, is prompting the development of surface patterning techniques. Although traditional techniques such as focused ion-beam patterning, electron-beam etching, or nanoimprint lithography have been widely used, their common drawback is the need for a resist or polymer process and, hence, numerous chemical, thermal, and etching associated steps, which will influence the properties of devices. The only two ways to avoid the expensive and contaminated top-down processes are self-assembly [105, 106] and stenciling [107–111].

#### 1.8.1

##### Self-Assembled Nanoscale Structures

Self-assembly process allows to pattern large-area arrays of high quality, possible epitaxial nanostructure with lateral dimensions at the nanoscale, in the sub-100 nm range. The self-assembled nanoscale structure is a good platform for in-depth investigation of the effects induced by defects and size on structural quality and properties. Ordered self-assembly complex oxide Ce:BaTiO<sub>3</sub> quantum dots shaped as a pyramid with a square base were fabricated by PLD, and the nonlinear effect is improved by the low-dimensional structures [112].

#### 1.8.2

##### Geometrically Ordered Arrays

Well-ordered arrays of nanoscale complex oxide structures without using the classic top-down process is technically very demanding. A stencil mask, which is a pattern of apertures in a thin free-standing membrane, is developed to fabricate geometrically ordered arrays [13, 113]. A nanoscale-ordered arrays of BaTiO<sub>3</sub> thin films in a single deposition step by PLD is achieved through nanostencil.

The nanostencil method is quite easy and elegant, but it suffers from a few disadvantages, such as the lack of long-range order and the individual final size. Lee *et al.* have developed an alternative mask. They used porous anodic alumina oxide (AAO) as template and electrodeposition to make gold nanotube membranes, which is used as a stencil mask for the deposition of complex oxides nanostructure.

Perfectly, two-dimensional (2D) arrays of ferroelectric PZT nanodots (50 nm in diameter) were fabricated using PLD by ultrathin AAO membrane stencil masks to investigate vortex polarization states in nanoscale ferroelectric arrays [114].

## 1.9

### Variation of Pulsed Laser Deposition

As with most techniques, PLD has several variants. Most variations of PLD have been summarized by Gupta in 1994 [115]. Since then, several further adaptations have been presented. Combinatorial PLD extends the basic PLD setup to include multiple lasers and targets and currently shows great potential for precision materials engineering [116]. The combined setup can be used to grow designer materials or alloys with deliberately engineered physical properties [117] and enables greater control over film stoichiometry. Also, it can facilitate deposition of material that cannot currently be fabricated by conventional, single-laser, single-target PLD [118–120]. In addition, continuous compositional spread technique is based on PLD and applied to the growth of epitaxial films [121].

## 1.10

### Conclusion

PLD system is a very useful tool to fabricate high-quality complex oxide thin films and nanostructures because of the technical simplicity and the ease with which deposition can be switched from one material to another. The most important is that it can maintain the stoichiometric target material in the thin film.

Although the setup of PLD is simple, the operation principles are complex. Various factors can significantly influence the crystalline structure and physical properties of the complex oxide thin film and nanostructure, such as the substrate temperature, background gas, laser energy density, the target–substrate distance, post-annealing, and so on.

PLD can be used to fabricate various complex oxide thin films, for instance, high-temperature superconductor epitaxial thin film, high-quality ferroelectric and ferromagnetic thin film, and multiferroic single-phase thin film or horizontal/vertical heterostructures.

With the development of PLD system, there are a lot of variants of PLD. For example, a multiple lasers and target PLD system can fabricate designer materials or alloys with deliberately engineered physical properties and can even realize the deposition of material that cannot currently be fabricated by conventional, single-laser, single-target PLD.

Like any deposition technique, PLD has some weaknesses, but it is a promising research tool for investigating new growth phenomena and systems, offering some new and unique features.

## References

1. Ozgur, U., Alivov, Y.I., Liu, C., Teke, A., Reshchikov, M.A., Dogan, S., Avrutin, V., Cho, S.J., and Morkoc, H. (2005) A comprehensive review of ZnO materials and devices. *J. Appl. Phys.*, **98**, 041301.
2. Kim, H., Gilmore, C.M., Pique, A., Horwitz, J.S., Mattoussi, H., Murata, H., Kafafi, Z.H., and Chrisey, D.B. (1999) Electrical, optical, and structural properties of indium-tin-oxide thin films for organic light-emitting devices. *J. Appl. Phys.*, **86**, 6451–6461.
3. Janotti, A. and Van de Walle, C.G. (2009) Fundamentals of zinc oxide as a semiconductor. *Rep. Prog. Phys.*, **72**, 126501.
4. Choi, D.H., Lee, D., Sim, H., Chang, M., and Hwang, H.S. (2006) Reversible resistive switching of SrTiO<sub>x</sub> thin films for nonvolatile memory applications. *Appl. Phys. Lett.*, **88**, 082904.
5. Panda, D. and Tseng, T.Y. (2013) Growth, dielectric properties, and memory device applications of ZrO<sub>2</sub> thin films. *Thin Solid Films*, **531**, 1–20.
6. Liu, J., Liu, M., Collins, G., Chen, C.L., Jiang, X.N., Gong, W.Q., Jacobson, A.J., He, J., Jiang, J.C., and Meletis, E.I. (2010) Epitaxial nature and transport properties in LaBaCo<sub>2</sub>O<sub>5+δ</sub> thin films. *Chem. Mater.*, **22**, 799–802.
7. Liu, M., Ren, S.P., Zhang, R.Y., Xue, Z.Y., Ma, C.R., Yin, M.L., Xu, X., Bao, S.Y., and Chen, C.L. (2015) Gas sensing properties of epitaxial LaBaCo<sub>2</sub>O<sub>5.5+δ</sub> thin films. *Sci. Rep.-UK*, **5**, 10784.
8. Smith, H.M. and Turner, A.F. (1965) Vacuum Deposited Thin Films Using a Ruby Laser. *Appl. Opt.*, **4**, 147–148.
9. Schwarz, H. and Tourtell, H. (1969) Vacuum deposition by high-energy laser with emphasis on barium titanate films. *J. Vac. Sci. Technol.*, **6**, 373–378.
10. Desserre, J. and Eloy, J.F. (1975) Interaction of pulsed coherent light-beam with complex target – Application to production of thin-film compounds. *Thin Solid Films*, **29**, 29–41.
11. Dijkkamp, D., Venkatesan, T., Wu, X.D., Shaheen, S.A., Jisrawi, N., Minlee, Y.H., Mclean, W.L., and Croft, M. (1987) Preparation of Y-Ba-Cu oxide superconductor thin-films using pulsed laser evaporation from high-Tc bulk material. *Appl. Phys. Lett.*, **51**, 619–621.
12. Zheng, H., Wang, J., Mohaddes-Ardabili, L., Wuttig, M., Salamanca-Riba, L., Schlom, D.G., and Ramesh, R. (2004) Three-dimensional heteroepitaxy in self-assembled BaTiO<sub>3</sub>-CoFe<sub>2</sub>O<sub>4</sub> nanostructures. *Appl. Phys. Lett.*, **85**, 2035–2037.
13. Cojocaru, C.V., Harnagea, C., Rosei, F., Pignolet, A., van den Boogaart, M.A.F., and Brugger, J. (2005) Complex oxide nanostructures by pulsed laser deposition through nanostencils. *Appl. Phys. Lett.*, **86**, 183107.
14. Ji, Y.D., Zhang, Y., Gao, M., Yuan, Z., Xia, Y.D., Jin, C.Q., Tao, B.W., Chen, C.L., Jia, Q.X., and Lin, Y. (2014) Role of microstructures on the M1-M2 phase transition in epitaxial VO<sub>2</sub> thin films. *Sci. Rep.-UK*, **4**, 4854.
15. Izyumskaya, N., Alivov, Y., Cho, S.J., Morkoc, H., Lee, H., and Kang, Y.S. (2007) Processing, structure, properties, and applications of PZT thin films. *Crit. Rev. Solid State Mater. Sci.*, **32**, 111–202.
16. Zhou, Y.C., Cao, W.J., Liu, L.C., Agaian, S., and Chen, C.L.P. (2015) Fast Fourier transform using matrix decomposition. *Inf. Sci.*, **291**, 172–183.
17. Martin, L.W., Chu, Y.H., and Ramesh, R. (2010) Advances in the growth and characterization of magnetic, ferroelectric, and multiferroic oxide thin films. *Mater. Sci. Eng., R*, **68**, 89–133.
18. Ohnishi, T., Yamamoto, T., Meguro, S., Koinuma, H., and Lippmaa, M. (2007) Pulsed laser ablation and deposition of complex oxides. *J. Phys. Conf. Ser.*, **59**, 514–519.
19. Singh, R.K. and Narayan, J. (1990) Pulsed-laser evaporation technique for deposition of thin films: physics and theoretical model. *Phys. Rev. B*, **41**, 8843–8859.
20. Willmott, P.R. and Huber, J.R. (2000) Pulsed laser vaporization and deposition. *Rev. Mod. Phys.*, **72**, 315–328.

21. Ratsch, C. and Venables, J.A. (2003) Nucleation theory and the early stages of thin film growth. *J. Vac. Sci. Technol., A*, **21**, S96–S109.
22. Venables, J.A., Spiller, G.D.T., and Hanbucken, M. (1984) Nucleation and growth of thin-films. *Rep. Prog. Phys.*, **47**, 399–459.
23. Vook, R.W. (1984) Nucleation and growth of thin-films. *Opt. Eng.*, **23**, 343–348.
24. Markov, I. and Kaischew, R. (1976) Influence of supersaturation on mode of crystallization on crystalline substrates. *Thin Solid Films*, **32**, 163–167.
25. Reichelt, K. (1988) Nucleation and growth of thin-films. *Vacuum*, **38**, 1083–1099.
26. Metev, S. and Meteva, K. (1989) Nucleation and growth of laser-plasma deposited thin-films. *Appl. Surf. Sci.*, **43**, 402–408.
27. Klein, J., Hofener, C., Alff, L., and Gross, R. (1999) *In situ* monitoring of the growth of oxide thin films at high oxygen pressure. *Supercond. Sci. Technol.*, **12**, 1023–1026.
28. Rijnders, G., Koster, G., Blank, D.H.A., and Rogalla, H. (1997) *In situ* monitoring during pulsed laser deposition of complex oxides using reflection high energy electron diffraction under high oxygen pressure. *Appl. Phys. Lett.*, **70**, 1888–1890.
29. Huijben, M., Brinkman, A., Koster, G., Rijnders, G., Hilgenkamp, H., and Blank, D.H.A. (2009) Structure-property relation of SrTiO<sub>3</sub>/LaAlO<sub>3</sub> interfaces. *Adv. Mater.*, **21**, 1665–1677.
30. Tischler, J., Eres, G., Larson, B., Rouleau, C.M., Zschack, P., and Lowndes, D.H. (2006) Nonequilibrium interlayer transport in pulsed laser deposition. *Phys. Rev. Lett.*, **96**, 226104.
31. Braun, W., Jenichen, B., Kaganer, V.M., Shtukenberg, A.G., Daweritz, L., and Ploog, K.H. (2003) Layer-by-layer growth of GaAs(001) studied by *in situ* synchrotron X-ray diffraction. *Surf. Sci.*, **525**, 126–136.
32. Ohring, M. (1991) *The Materials Science of Thin Films*, Academic Press, Inc.
33. Sambri, A., Amoruso, S., Wang, X., Radovic, M., Granozio, F.M., and Bruzzese, R. (2007) Substrate heating influence on plume propagation during pulsed laser deposition of complex oxides. *Appl. Phys. Lett.*, **91**, 151501.
34. Willmott, P.R. (2004) Deposition of complex multielemental thin films. *Prog. Surf. Sci.*, **76**, 163–217.
35. Sturm, K., Fahler, S., and Krebs, H.U. (2000) Pulsed laser deposition of metals in low pressure inert gas. *Appl. Surf. Sci.*, **154**, 462–466.
36. Scharf, T. and Krebs, H.U. (2002) Influence of inert gas pressure on deposition rate during pulsed laser deposition. *Appl. Phys. A-Mater. Sci. Process.*, **75**, 551–554.
37. Yang, W.Q., Wei, Z.R., Gao, M., Chen, Y., Xu, J., Chen, C.L., and Lin, Y. (2013) Fabrication and field emission properties of needle-shaped MoO<sub>3</sub> nanobelts. *J. Alloys Compd.*, **576**, 332–335.
38. Ohnishi, T., Lippmaa, M., Yamamoto, T., Meguro, S., and Koinuma, H. (2005) Improved stoichiometry and misfit control in perovskite thin film formation at a critical fluence by pulsed laser deposition. *Appl. Phys. Lett.*, **87**, 241919.
39. Ohnishi, T., Shibuya, K., Yamamoto, T., and Lippmaa, M. (2008) Defects and transport in complex oxide thin films. *J. Appl. Phys.*, **103**, 103703.
40. Ngom, B.D., Lafane, S., Dioum, A., Manyala, N., Abdelli-Messaci, S., Kerdja, R.T., Madjoe, R., Nemitudi, R., Maaza, M., and Beye, A.C. (2011) The influence of plasma dynamics on the growth of Sm<sub>0.55</sub>Nd<sub>0.45</sub>NiO<sub>3</sub> solid solution during pulsed laser deposition. *J. Phys. Chem. Solids*, **72**, 1218–1224.
41. Claeysens, F., Cheesman, A., Henley, S.J., and Ashfold, M.N.R. (2002) Studies of the plume accompanying pulsed ultraviolet laser ablation of zinc oxide. *J. Appl. Phys.*, **92**, 6886–6894.
42. Hammond, R.H. and Bormann, R. (1989) Correlation between the *in situ* growth-conditions of YBCO thin-films and the thermodynamic stability-criteria. *Physica C*, **162**, 703–704.
43. Kim, H.S. and Kwok, H.S. (1992) Correlation between target-substrate distance

- and oxygen-pressure in pulsed laser deposition of  $\text{YBa}_2\text{Cu}_3\text{O}_7$ . *Appl. Phys. Lett.*, **61**, 2234–2236.
44. Castro-Rodriguez, R., Coronado, D.R., Iribarren, A., Watts, B.E., Leccabue, F., and Pena, J.L. (2005) Correlation between target-substrate distance and oxygen pressure in pulsed laser deposition of complex oxide thin films. *Appl. Phys. A*, **81**, 1503–1507.
  45. Pan, F., Song, C., Liu, X.J., Yang, Y.C., and Zeng, F. (2008) Ferromagnetism and possible application in spintronics of transition-metal-doped ZnO films. *Mater. Sci. Eng., R*, **62**, 1–35.
  46. Rusop, M., Uma, K., Soga, T., and Jimbo, T. (2006) Post-growth annealing of zinc oxide thin films pulsed laser deposited under enhanced oxygen pressure on quartz and silicon substrates. *Mater. Sci. Eng., B*, **127**, 150–153.
  47. Liu, M., Ma, C.R., Enriquez, E., Xu, X., Bao, S.Y., and Chen, C.L. (2014) Effects of annealing ambient on electrical properties of  $\text{LaBaCo}_2\text{O}_{5+\delta}$  thin films. *J. Nano Res.-Sw*, **27**, 25–30.
  48. Liu, M., Ma, C.R., Liu, J., Collins, G., Chen, C.L., He, J., Jiang, J.C., Meletis, E.I., Sun, L., Jacobson, A.J., and Whangbo, M.H. (2012) Giant magnetoresistance and anomalous magnetic properties of highly epitaxial ferromagnetic  $\text{LaBaCo}_2\text{O}_{5.5+\delta}$  thin films on (001) MgO. *ACS Appl. Mater. Interfaces*, **4**, 5524–5528.
  49. Hundley, M.F., Hawley, M., Heffner, R.H., Jia, Q.X., Neumeier, J.J., Tesmer, J., Thompson, J.D., and Wu, X.D. (1995) Transport-magnetism correlations in the ferromagnetic oxide  $\text{La}_{0.7}\text{Ca}_{0.3}\text{MnO}_3$ . *Appl. Phys. Lett.*, **67**, 860–862.
  50. Opel, M. (2012) Spintronic oxides grown by laser-MBE. *J. Phys. D: Appl. Phys.*, **45**, 033001.
  51. Roas, B., Schultz, L., and Endres, G. (1988) Epitaxial-growth of  $\text{YBa}_2\text{Cu}_3\text{O}_{7-x}$  thin-films by a laser evaporation process. *Appl. Phys. Lett.*, **53**, 1557–1559.
  52. Buzea, C. and Yamashita, T. (2001) Review of the superconducting properties of  $\text{MgB}_2$ . *Supercond. Sci. Technol*, **14**, R115–R146.
  53. Yamada, Y., Takahashi, K., Kobayashi, H., Konishi, M., Watanabe, T., Ibi, A., Muroga, T., Miyata, S., Kato, T., Hirayama, T., and Shiohara, Y. (2005) Epitaxial nanostructure and defects effective for pinning in  $\text{Y}(\text{RE})\text{Ba}_2\text{Cu}_3\text{O}_{7-x}$  coated conductors. *Appl. Phys. Lett.*, **87**, 132502.
  54. Lee, P.A., Nagaosa, N., and Wen, X.G. (2006) Doping a Mott insulator: physics of high-temperature superconductivity. *Rev. Mod. Phys.*, **78**, 17–85.
  55. Norton, D.P., Goyal, A., Budai, J.D., Christen, D.K., Kroeger, D.M., Specht, E.D., He, Q., Saffian, B., Paranthaman, M., Klabunde, C.E., Lee, D.F., Sales, B.C., and List, F.A. (1996) Epitaxial  $\text{YBa}_2\text{Cu}_3\text{O}_7$  on biaxially textured nickel (001): an approach to superconducting tapes with high critical current density. *Science*, **274**, 755–757.
  56. Locquet, J.P., Perret, J., Fompeyrine, J., Machler, E., Seo, J.W., and Van Tendeloo, G. (1998) Doubling the critical temperature of  $\text{La}_{1.9}\text{Sr}_{0.1}\text{CuO}_4$  using epitaxial strain. *Nature*, **394**, 453–456.
  57. Miura, S., Yoshida, Y., Ichino, Y., Matsumoto, K., Ichinose, A., and Awaji, S. (2015) Characteristics of high-performance  $\text{BaHfO}_3$ -doped  $\text{SmBa}_2\text{Cu}_3\text{O}_y$  superconducting films fabricated with a seed layer and low-temperature growth. *Supercond. Sci. Technol.*, **28**, 065013.
  58. Dawber, M., Rabe, K.M., and Scott, J.F. (2005) Physics of thin-film ferroelectric oxides. *Rev. Mod. Phys.*, **77**, 1083–1130.
  59. Setter, N., Damjanovic, D., Eng, L., Fox, G., Gevorgian, S., Hong, S., Kingon, A., Kohlstedt, H., Park, N.Y., Stephenson, G.B., Stolitchnov, I., Tagantsev, A.K., Taylor, D.V., Yamada, T., and Streiffer, S. (2006) Ferroelectric thin films: review of materials, properties, and applications. *J. Appl. Phys.*, **100**, 051606.
  60. Lee, H.N., Hesse, D., Zakharov, N., and Gosele, U. (2002) Ferroelectric  $\text{Bi}_{3.25}\text{La}_{0.75}\text{Ti}_3\text{O}_{12}$  films of uniform *a*-axis orientation on silicon substrates. *Science*, **296**, 2006–2009.
  61. Scott, J.F. (1998) High-dielectric constant thin films for dynamic random

- access memories (DRAM). *Annu. Rev. Mater. Sci.*, **28**, 79–100.
62. Prins, M.W.J., GrosseHolz, K.O., Muller, G., Cillessen, J.F.M., Giesbers, J.B., Weening, R.P., and Wolf, R.M. (1996) A ferroelectric transparent thin-film transistor. *Appl. Phys. Lett.*, **68**, 3650–3652.
  63. Watanabe, Y., Tanamura, M., Matsumoto, Y., Asami, H., and Kato, A. (1995) Ferroelectric (La,Sr)(2)CuO<sub>4</sub> epitaxial heterostructure with high thermal-stability. *Appl. Phys. Lett.*, **66**, 299–301.
  64. Ramesh, R., Inam, A., Chan, W.K., Wilkens, B., Myers, K., Remschnig, K., Hart, D.L., and Tarascon, J.M. (1991) Epitaxial cuprate superconductor ferroelectric heterostructures. *Science*, **252**, 944–946.
  65. Liu, M., Collins, G., Silva, E., Ma, C.R., Liu, J., Chen, C.L., He, J., Jiang, J.C., Meletis, E.I., Qu, S.W., Zhang, Q.Y., and Bhalla, A. (2011) Interface engineered ferroelectric BaTiO<sub>3</sub>/SrTiO<sub>3</sub> heterostructures with anomalous clamped polarization on Si (100). *Integr. Ferroelectr.*, **131**, 89–94.
  66. Liu, M., Liu, J., Ma, C.R., Collins, G., Chen, C.L., Alemayehu, A.D., Subramanyam, G., He, J., Jiang, J.C., Meletis, E.I., and Bhalla, A. (2013) Enhanced dielectric properties of (Ba, Sr)TiO<sub>3</sub>//Ba(Zr, Ti)O<sub>3</sub> heterostructures with optimized structure design. *CrystEngComm*, **15**, 6641–6644.
  67. Liu, M., Ma, C.R., Collins, G., Liu, J., Chen, C.L., Alemayehu, A.D., Subramanyam, G., Ding, Y., Chen, J.H., Dai, C., Lin, Y., and Cole, M.W. (2013) Ferroelectric BaTiO<sub>3</sub>/SrTiO<sub>3</sub> multilayered thin films for room-temperature tunable microwave elements. *Nanoscale Res. Lett.*, **8**, 338.
  68. Liu, M., Ma, C.R., Collins, G., Liu, J., Chen, C.L., Dai, C., Lin, Y., Shui, L., Xiang, F., Wang, H., He, J., Jiang, J.C., Meletis, E.I., and Cole, M.W. (2012) Interface engineered BaTiO<sub>3</sub>/SrTiO<sub>3</sub> heterostructures with optimized high-frequency dielectric properties. *ACS Mater. Interfaces*, **4**, 5761–5765.
  69. Liu, M., Ma, C.R., Collins, G., Liu, J.A., Chen, C.L., Shui, L., Wang, H., Dai, C., Lin, Y.A., He, J., Jiang, J.C., Meletis, E.I., and Zhang, Q.Y. (2010) Microwave dielectric properties with optimized Mn-doped Ba<sub>0.6</sub>Sr<sub>0.4</sub>TiO<sub>3</sub> highly epitaxial thin films. *Cryst. Growth Des.*, **10**, 4221–4223.
  70. Liu, M., Ma, C.R., Liu, J., Collins, G., Chen, C.L., Xiang, F., Wang, H., He, J., Jiang, J.C., Meletis, E.I., and Bhalla, A. (2014) Microwave dielectric properties of Mn-doped (Ba, Sr)TiO<sub>3</sub>//Ba(Zr, Ti)O<sub>3</sub> multilayered thin films: optimization of designed structure. *Integr. Ferroelectr.*, **150**, 116–122.
  71. Schlom, D.G., Chen, L.Q., Eom, C.B., Rabe, K.M., Streiffer, S.K., and Triscone, J.M. (2007) Strain tuning of ferroelectric thin films. *Annu. Rev. Mater. Res.*, **37**, 589–626.
  72. Ueda, K., Tabata, H., and Kawai, T. (2001) Magnetic and electric properties of transition-metal-doped ZnO films. *Appl. Phys. Lett.*, **79**, 988–990.
  73. Haghiri-Gosnet, A.M. and Renard, J.P. (2003) CMR manganites: physics, thin films and devices. *J. Phys. D: Appl. Phys.*, **36**, R127–R150.
  74. Akahoshi, D. and Ueda, Y. (2001) Oxygen nonstoichiometry, structures, and physical properties of YBaCo<sub>2</sub>O<sub>5+x</sub> (0.00 ≤ x ≤ 0.52). *J. Solid State Chem.*, **156**, 355–363.
  75. Podlesnyak, A., Streule, S., Mesot, J., Medarde, M., Pomjakushina, E., Conder, K., Tanaka, A., Haverkort, M.W., and Khomskii, D.I. (2006) Spin-state transition in LaCoO<sub>3</sub>: direct neutron spectroscopic evidence of excited magnetic states. *Phys. Rev. Lett.*, **97**, 247208.
  76. Seikh, M.M., Simon, C., Caignaert, V., Pralong, V., Lepetit, M.B., Boudin, S., and Raveau, B. (2008) New magnetic transitions in the ordered oxygen-deficient perovskite LnBaCo<sub>2</sub>O<sub>5.5+δ</sub>. *Chem. Mater.*, **20**, 231–238.
  77. Ma, C.R., Liu, M., Collins, G., Liu, J., Zhang, Y.M., Chen, C.L., He, J., Jiang, J.C., and Meletis, E.I. (2012) Thickness effects on the magnetic and electrical transport properties of highly epitaxial LaBaCo<sub>2</sub>O<sub>5.5+δ</sub> thin films on MgO substrates. *Appl. Phys. Lett.*, **101**, 021602.

78. Ma, C.R., Liu, M., Collins, G., Wang, H.B., Bao, S.Y., Xu, X., Enriquez, E., Chen, C.L., Lin, Y., and Whangbo, M.H. (2013) Magnetic and electrical transport properties of LaBaCo<sub>2</sub>O<sub>5.5+δ</sub> thin films on vicinal (001) SrTiO<sub>3</sub> surfaces. *ACS Appl. Mater. Interfaces*, **5**, 451–455.
79. Ma, C.R., Liu, M., Liu, J., Collins, G., Zhang, Y.M., Wang, H.B., Chen, C.L., Lin, Y., He, J., Jiang, J.C., Meletis, E.I., and Jacobson, A.J. (2014) Interface effects on the electronic transport properties in highly epitaxial LaBaCo<sub>2</sub>O<sub>5.5+δ</sub> films. *ACS Appl. Mater. Interfaces*, **6**, 2540–2545.
80. Coey, J.M.D., Douvalis, A.P., Fitzgerald, C.B., and Venkatesan, M. (2004) Ferromagnetism in Fe-doped SnO<sub>2</sub> thin films. *Appl. Phys. Lett.*, **84**, 1332–1334.
81. Cheong, S.W. and Mostovoy, M. (2007) Multiferroics: a magnetic twist for ferroelectricity. *Nat. Mater.*, **6**, 13–20.
82. Ramesh, R. and Spaldin, N.A. (2007) Multiferroics: progress and prospects in thin films. *Nat. Mater.*, **6**, 21–29.
83. Fujimura, N., Azuma, S., Aoki, N., Yoshimura, T., and Ito, T. (1996) Growth mechanism of YMnO<sub>3</sub> film as a new candidate for nonvolatile memory devices. *J. Appl. Phys.*, **80**, 7084–7088.
84. Salvador, P.A., Doan, T.D., Mercey, B., and Raveau, B. (1998) Stabilization of YMnO<sub>3</sub> in a perovskite structure as a thin film. *Chem. Mater.*, **10**, 2592–2595.
85. Ueda, K., Tabata, H., and Kawai, T. (1999) Coexistence of ferroelectricity and ferromagnetism in BiFeO<sub>3</sub>-BaTiO<sub>3</sub> thin films at room temperature. *Appl. Phys. Lett.*, **75**, 555–557.
86. Palkar, V.R., John, J., and Pinto, R. (2002) Observation of saturated polarization and dielectric anomaly in magnetoelectric BiFeO<sub>3</sub> thin films. *Appl. Phys. Lett.*, **80**, 1628–1630.
87. Murugavel, P., Saurel, D., Prellier, W., Simon, C., and Raveau, B. (2004) Tailoring of ferromagnetic Pr<sub>0.85</sub>Ca<sub>0.15</sub>MnO<sub>3</sub>/ferroelectric Ba<sub>0.6</sub>Sr<sub>0.4</sub>TiO<sub>3</sub> superlattices for multiferroic properties. *Appl. Phys. Lett.*, **85**, 4424–4426.
88. Singh, M.P., Prellier, W., Simon, C., and Raveau, B. (2005) Magnetocapacitance effect in perovskite-superlattice based multiferroics. *Appl. Phys. Lett.*, **87**, 022505.
89. Zheng, H., Wang, J., Lofland, S.E., Ma, Z., Mohaddes-Ardabili, L., Zhao, T., Salamanca-Riba, L., Shinde, S.R., Ogale, S.B., Bai, F., Viehland, D., Jia, Y., Schlom, D.G., Wuttig, M., Roytburd, A., and Ramesh, R. (2004) Multiferroic BaTiO<sub>3</sub>-CoFe<sub>2</sub>O<sub>4</sub> nanostructures. *Science*, **303**, 661–663.
90. Yang, F., Kemik, N., Biegalski, M.D., Christen, H.M., Arenholz, E., and Takamura, Y. (2010) Strain engineering to control the magnetic and magnetotransport properties of La<sub>0.67</sub>Sr<sub>0.33</sub>MnO<sub>3</sub> thin films. *Appl. Phys. Lett.*, **97**, 092503.
91. Xiong, Y.M., Wang, G.Y., Luo, X.G., Wang, C.H., Chen, X.H., Chen, X., and Chen, C.L. (2005) Magnetotransport properties in La<sub>1-x</sub>Ca<sub>x</sub>MnO<sub>3</sub> (x=0.33, 0.5) thin films deposited on different substrates. *J. Appl. Phys.*, **97**, 083909.
92. Xiong, Y.M., Chen, T., Wang, G.Y., Chen, X.H., Chen, X., and Chen, C.L. (2004) Raman spectra in epitaxial thin films of La<sub>1-x</sub>Ca<sub>x</sub>MnO<sub>3</sub> (x=0.33, 0.5) grown on different substrates. *Phys. Rev. B*, **70**, 094407.
93. Park, S., Ryan, P., Karapetrova, E., Kim, J.W., Ma, J.X., Shi, J., Freeland, J.W., and Wu, W.D. (2009) Microscopic evidence of a strain-enhanced ferromagnetic state in LaCoO<sub>3</sub> thin films. *Appl. Phys. Lett.*, **95**, 072508.
94. Lin, Y., Dai, C., Li, Y.R., Chen, X., Chen, C.L., Bhalla, A., and Jia, Q.X. (2010) Strain relaxation in epitaxial (Pb,Sr)TiO<sub>3</sub> thin films on NdGaO<sub>3</sub> substrates. *Appl. Phys. Lett.*, **96**, 102901.
95. Grutter, A., Wong, F., Arenholz, E., Liberati, M., Vailionis, A., and Suzuki, Y. (2010) Enhanced magnetism in epitaxial SrRuO<sub>3</sub> thin films. *Appl. Phys. Lett.*, **96**, 082509.
96. Grutter, A., Wong, F., Arenholz, E., Liberati, M., and Suzuki, Y. (2010) Enhanced magnetization in epitaxial SrRuO<sub>3</sub> thin films via substrate-induced strain. *J. Appl. Phys.*, **107**, 09e138.

97. Millis, A.J., Darling, T., and Migliori, A. (1998) Quantifying strain dependence in “colossal” magnetoresistance manganites. *J. Appl. Phys.*, **83**, 1588–1591.
98. Radaelli, P.G., Iannone, G., Marezio, M., Hwang, H.Y., Cheong, S.W., Jorgensen, J.D., and Argyriou, D.N. (1997) Structural effects on the magnetic and transport properties of perovskite  $A_{1-x}A_xMnO_3$  ( $x = 0.25, 0.30$ ). *Phys. Rev. B*, **56**, 8265–8276.
99. Kundu, A.K., Raveau, B., Caignaert, V., Rautama, E.L., and Pralong, V. (2009) Electron transport and thermoelectric properties of layered perovskite  $LaBaCo_2O_{5.5}$ . *J. Phys.: Condens. Matter*, **21**, 056007.
100. Rautama, E.L., Boullay, P., Kundu, A.K., Caignaert, V., Pralong, V., Karppinen, M., and Raveau, B. (2008) Cationic ordering and microstructural effects in the ferromagnetic perovskite  $La_{0.5}Ba_{0.5}CoO_3$ : impact upon magnetotransport properties. *Chem. Mater.*, **20**, 2742–2750.
101. Liu, M., Liu, J., Collins, G., Ma, C.R., Chen, C.L., He, J., Jiang, J.C., Meletis, E.I., Jacobson, A.J., and Zhang, Q.Y. (2010) Magnetic and transport properties of epitaxial  $LaBaCo_2O_{5.5+\delta}$  thin films on (001)  $SrTiO_3$ . *Appl. Phys. Lett.*, **96**, 132106.
102. Jiang, J.C., Lin, Y., Chen, C.L., Chu, C.W., and Meletis, E.I. (2002) Microstructures and surface step-induced antiphase boundaries in epitaxial ferroelectric  $Ba_{0.6}Sr_{0.4}TiO_3$  thin film on  $MgO$ . *J. Appl. Phys.*, **91**, 3188–3192.
103. Lu, H.L., Zhang, C.D., Guo, H.M., Gao, H.J., Liu, M., Liu, J.A., Collins, G., and Chen, C.L. (2010) Surface-step-terrace-induced anomalous transport properties in highly epitaxial  $La_{0.67}Ca_{0.33}MnO_3$  thin films. *ACS Appl. Mater. Interfaces*, **2**, 2496–2499.
104. Raveau, B., Pralong, V., Caignaert, V., Hervieu, M., and Maignan, A. (2005) Primordial role of cobalt valence in the magnetotransport properties of oxygen deficient perovskites  $Sr_{1-x}Ln_xCoO_{3-\delta}$ . *J. Phys.: Condens. Matter*, **17**, 7371–7382.
105. Szafraniak, I., Harnagea, C., Scholz, R., Bhattacharyya, S., Hesse, D., and Alexe, M. (2003) Ferroelectric epitaxial nanocrystals obtained by a self-patterning method. *Appl. Phys. Lett.*, **83**, 2211–2213.
106. Roelofs, A., Schneller, I., Szot, K., and Waser, R. (2002) Piezoresponse force microscopy of lead-titanate nanograins possibly reaching the limit of ferroelectricity. *Appl. Phys. Lett.*, **81**, 5231–5233.
107. Lee, W., Han, H., Lotnyk, A., Schubert, M.A., Senz, S., Alexe, M., Hesse, D., Baik, S., and Gosele, U. (2008) Individually addressable epitaxial ferroelectric nanocapacitor arrays with near Tb inch(-2) density. *Nat. Nanotechnol.*, **3**, 402–407.
108. Lee, W., Schwirn, K., Steinhart, M., Pippel, E., Scholz, R., and Gosele, U. (2008) Structural engineering of nanoporous anodic aluminium oxide by pulse anodization of aluminium. *Nat. Nanotechnol.*, **3**, 234–239.
109. Lee, S.K., Lee, W., Alexe, M., Nielsch, K., Hesse, D., and Gosele, U. (2005) Well-ordered large-area arrays of epitaxial ferroelectric  $(Bi,La)_4Ti_3O_{12}$  nanostructures fabricated by gold nanotube-membrane lithography. *Appl. Phys. Lett.*, **86**, 152906.
110. Shin, H.J., Choi, J.H., Yang, H.J., Park, Y.D., Kuk, Y., and Kang, C.J. (2005) Patterning of ferroelectric nanodot arrays using a silicon nitride shadow mask. *Appl. Phys. Lett.*, **87**, 113114.
111. Vrejoiu, I., Alexe, M., Hesse, D., and Gosele, U. (2008) Functional perovskites – From epitaxial films to nanostructured arrays. *Adv. Funct. Mater.*, **18**, 3892–3906.
112. Shi, W.S., Chen, Z.H., Liu, N.N., Lu, H.B., Zhou, Y.L., Cui, D.F., and Yang, G.Z. (1999) Nonlinear optical properties of self-organized complex oxide  $Ce:BaTiO_3$  quantum dots grown by pulsed laser deposition. *Appl. Phys. Lett.*, **75**, 1547–1549.
113. Cojocaru, C.-V., Nechache, R., Harnagea, C., Pignolet, A., and Rosei, F. (2010) Nanoscale patterning of functional perovskite-type complex oxides by pulsed laser deposition through a nanostencil. *Appl. Surf. Sci.*, **256**, 4777–4783.

114. Rodriguez, B.J., Gao, X.S., Liu, L.F., Lee, W., Naumov, I.I., Bratkovsky, A.M., Hesse, D., and Alexe, M. (2009) Vortex polarization states in nanoscale ferroelectric arrays. *Nano Lett.*, **9**, 1127–1131.
115. Gupta, A., Chrisey, D.B., and Hubler, G.K. (1994) *Pulsed Laser Deposition of Thin Films*, Wiley-Interscience, New York.
116. Sloyan, K.A., May-Smith, T.C., Eason, R.W., and Lunney, J.G. (2009) The effect of relative plasma plume delay on the properties of complex oxide films grown by multi-laser, multi-target combinatorial pulsed laser deposition. *Appl. Surf. Sci.*, **255**, 9066–9070.
117. Gazia, R., May-Smith, T.C., and Eason, R.W. (2008) Growth of a hybrid garnet crystal multilayer structure by combinatorial pulsed laser deposition. *J. Cryst. Growth*, **310**, 3848–3853.
118. Darby, M.S.B., May-Smith, T.C., and Eason, R.W. (2008) Deposition and stoichiometry control of Nd-doped gadolinium gallium garnet thin films by combinatorial pulsed laser deposition using two targets of Nd:  $Gd_3Ga_5O_{12}$  and  $Ga_2O_3$ . *Appl. Phys. A*, **93**, 477–481.
119. Holesinger, T.G., Jia, Q., Maiorov, B., Civale, L., Dowden, P.C., and Gibbons, B.J. (2007) Ultrafine multilayers of complex metal oxide films. *Adv. Mater.*, **19**, 1917–1920.
120. Willmott, P.R., Herger, R., and Schleputz, C.M. (2004) Multilayers, alloys, and complex profiles by pulsed laser deposition using a novel target geometry. *Thin Solid Films*, **453**, 436–439.
121. Christen, H.M., Silliman, S.D., and Harshavardhan, K.S. (2001) Continuous compositional-spread technique based on pulsed-laser deposition and applied to the growth of epitaxial films. *Rev. Sci. Instrum.*, **72**, 2673–2678.

